PHYSICAL REVIEW B **108**, 245416 (2023)

Coexistence of out-of-plane and in-plane ferroelectricity in ultrathin elemental group-V nanotube arrays

Yuwen Zhang,[*] Chunfeng Cui,[*] Chaoyu He,[†] Tao Ouyang,[‡] Jin Li, and Chao Tang[§]
Hunan Key Laboratory for Micro-Nano Energy Materials and Device and School of Physics and Optoelectronics, Xiangtan University, Xiangtan 411105, Hunan, China

(Received 26 August 2023; accepted 4 December 2023; published 18 December 2023)

The rare and abnormal elemental ferroelectricity has been predicted and realized in group-V monolayers in recent years [Xiao *et al.*, Adv. Funct. Mater. **28**, 1707383 (2018); Gou, Nature (London) **617**, 67 (2023)]. However, the valuable out-of-plane (OOP) ferroelectricity is missing in these monolayers owing to the symmetry of the glide plane. In this article, the low-energy nanotube arrays (NTs) of group-V elements (P, As, Sb, and Bi) are carefully confirmed to be ferroelectric materials with both OOP (0.15–0.43 pC/m) and in-plane (IP, 0.52–6.63 pC/m) spontaneous polarizations. The spontaneous polarization originates from the asymmetric electron distribution caused by the noncentrosymmetric tubular crystal structure. Meanwhile, benefited by the coexistence of OOP and IP polarizations, such tubular crystal structure also exhibits unique quadruple polarization states. The lower switching barriers between the logic states (ranging from 13 to 93 meV/atom) further indicate that they are easily controlled by external electric fields, facilitating efficient data read and write operations. These characteristics lay the foundation for their application in high-speed, low-power, and large-scale data storage. More interestingly, our calculations demonstrate that these NTs of group-V elements possess not only IP piezoelectricity comparable to MoS_2 (0.95–7.97 pm/V) but also nonzero OOP piezoelectric coefficients (0.04–8.01 pm/V), further expanding their potential applications in energy conversion. It is anticipated that these discoveries will undoubtedly serve to catalyze further research and applications involving single-element materials within the domains of ferroelectricity-based information storage and piezoelectricity-based energy conversion.

DOI: 10.1103/PhysRevB.108.245416

I. INTRODUCTIONS

Ferroelectric materials possess spontaneous polarization which can be reversed by electric field. This reversible polarization transition between dual- or multipolarization states can be utilized in nanoelectronic devices such as nonvolatile memories, piezoelectric sensors, and logic devices [1–3]. Since the discovery of ferroelectricity by Valasek [4] in single crystal Rochelle salt in 1920, the development of ferroelectric materials has gone through four stages: Rochelle salt, KH_2PO_4, perovskite, and ferroelectric thin film and device period [3,5]. Among them, the discovery of perovskite-structured ferroelectric materials represented by $BaTiO_3$ plays a milestone role in the development of ferroelectricity. With the rapid progress in microelectronics technology, there is an urgent demand for nonvolatile memories with low power consumption, fast read/write speed, and high reliability. Ferroelectric thin films [6–8] have attracted extensive research attention due to their potential for device miniaturization and numerous experiments have been performed to achieve ferroelectricity in perovskite structures at the two-dimensional (2D) limit [9,10]. However, conventional ferroelectric materials will lose their ferroelectric properties when they are downscaled to the nanoscale due to the influence of surface dangling bonds and depolarization fields [11]. In contrast, 2D van der Waals layered ferroelectric materials lack surface dangling bonds, which facilitates device miniaturization and improves device reliability and durability, and is a future trend in ferroelectric development [12,13].

2D semiconductor materials with both out-of-plane (OOP) or in-plane (IP) ferroelectric/piezoelectric properties are widely regarded as the optimal choice for realizing ultrathin ferroelectric/piezoelectric devices. In recent years, various 2D layered materials have been theoretically and experimentally reported as ferroelectric materials, for instance thin films of SnTe [14], 2D III_2-VI_3 compounds such as In_2Se_3 [15,16], $CuInP_2S_6$ [17,18], 1T-MoS_2 [19], MX [14,20–23] (M = Ge, Sn; X = S, Se, Te), chemically functionalized 2D materials [24,25], and 2D sliding ferroelectrics formed by van der Waals stacking [26–30]. The formation of chemical bonds in these materials triggers an instantaneous redistribution of electron density, leading to the generation of anionic and cationic centers. Therefore, ferroelectric materials usually need to contain several elements with significant differences in electronegativity and the elemental ferroelectricity is cognitively prohibited. In fact, whether a material hosts polarization, specific crystalline point group (1, 2, *m*, *mm*2, 4, 4*mm*, 3, 3*m*, 6, and 6*mm*) is the decisive factor [31]. These point groups are not

---

[*] These authors contributed equally to this work.
[†] hechaoyu@xtu.edu.cn
[‡] ouyangtao@xtu.edu.cn
[§] tang_chao@xtu.edu.cn

exclusive to multielement compounds. Recently, Xiao [32] and colleagues have predicted a puckered structure for As, Sb, and Bi with a noncentrosymmetric configuration and present IP ferroelectric polarization along the tangential direction. It should be noted here that the puckered structures of Bi element were recently synthesized successfully and confirmed to be elemental ferroelectric materials by the IP electric field generated by scanning probe microscopy [33].

The journey from theoretical predictions to experimental validation of elemental ferroelectricity is undeniably captivating. However, the presence of valuable OOP ferroelectricity is impeded in these monolayers due to the symmetry of the *mm*2 point group. Therefore, beyond the existence of IP ferroelectricity, the possibility of achieving OOP ferroelectricity or the coexistence of both IP and OOP ferroelectric spontaneous polarization in materials composed of individual elements is a subject well worth exploring. In a previous study, Liu *et al.* [34] theoretically introduced a unique type of ultrathin stable phosphorus nanotube, sharing fundamental structural units that closely resemble violet phosphorene [35,36] and fibrous red phosphorus [37]. Subsequently, Zhang *et al.* [38] experimentally demonstrated that ring-shaped phosphorus consisting of alternating P_8 and P_2 structural units could be assembled inside multiwall carbon nanotube nanoreactors with an inner diameter of 5–8 nm by a chemical vapor transport and reaction of red phosphorus at 500 °C. Intriguingly, Li *et al.* [39] have further shown that the interlamination between graphene layers could serve as an effective reactor for assembling these phosphorus nanotubes into 2D arrays and revealing inherent piezoelectric properties. These discoveries unarguably fortify our confidence in the pursuit of elemental ferroelectrics.

Asymmetric phosphorus nanotubes exhibit electric dipole behavior and their assembly into dipole arrays has the capacity to generate ferroelectricity. Given the analogous bonding characteristics of group-V elements, we performed a systematic investigation about the ferroelectric and piezoelectric properties of 2D nanotube arrays (NTs) comprised of individual group-V elements (P, As, Sb, and Bi). These NTs are demonstrated to possess remarkable IP and OOP spontaneous polarization, featuring with four equivalent polarized states capable of interconversion. Their room-temperature ferroelectric nature is further verified based on *ab initio* molecular dynamics (AIMD) simulations. Meanwhile, the presence of OOP piezoelectricity augments their potential utility in piezoelectric devices. The finding presented in this study represents a significant advancement in the realm of elemental ferroelectric materials and underscores the promise of group-V element-based ferroelectric NTs as promising candidates for future information storage applications.

II. COMPUTATIONAL METHODOLOGY

First-principles calculations based on density functional theory (DFT) are performed using the Vienna *ab initio* simulation package [40] (VASP) code. The interaction between ions and valence electrons is delineated using the projected augmented wave [41,42] (PAW) method. The exchange-correlation functional employs the generalized gradient approximation Perdew-Burke-Ernzerhof (GGA-PBE) functional [42,43]. The valence electrons of P, As, Sb, and Bi atoms are $3s^23p^3$, $4s^24p^3$, $5s^25p^3$, and $6s^25d^{10}6p^3$, respectively. The plane wave cutoff energy is set to 500 eV and the Monkhorst-Pack [44] method with Γ center is used to sample the first Brillouin zone. The spacing of k-point grids in reciprocal space is controlled within $0.02 \times 2\pi$ Å^{-1} by the VASPKIT [45] code. Throughout the optimization process, the convergence accuracy for energy and forces is set at 10^{-8} eV and 10^{-3} eV/Å precisely, ensuring substantial system optimization. The vacuum layer thickness is at least 15 Å to avoid periodic mirror interactions along the z direction. All geometry optimizations consider the van der Waals (vdW) correction using the Grimme-D2 [46] method. Berry's phase [47,48] method is employed for the evaluation of ferroelectric polarization. The density functional perturbation theory (DFPT) [49] method is used to calculate the piezoelectric stress coefficient e_{ij}. The Heyd-Scuseria-Ernzerhof [50] (HSE06) hybrid functional is selected for band structure computations. The ferroelectric switching barrier is obtained using the climbing image nudged elastic band [51] (CINEB) method. The PHONOPY [52] package is used to obtain phonon spectra by employing the finite displacement method on a $2 \times 3 \times 1$ supercell in order to verify dynamic stability. *Ab initio* molecular dynamics (AIMD) simulations are initiated at a temperature of 300 K for 10 ps with a 1 fs time step to examine the thermal stability and evaluate the ferroelectric failure temperature. In this calculation, we set the ensemble as isobar-isotherm ensemble (NPT) and the supercell size as $2 \times 3 \times 1$ (which contains 120 atoms).

III. RESULTS AND DISCUSSION

The crystal structure investigated in the present work for P, As, Sb, and Bi are composed of pentagons and each fundamental structural unit contains 10 atoms, as shown in Fig. 1(a). It closely resembles the basic structural units in violet phosphorene [35,36] and fibrous red phosphorus [37]. As illustrated in Fig. 1(b), the 2D NTs are constructed by assembling the individual nanotubes along the lattice direction a. The spacing between each nanotube is determined by the magnitude of van der Waals interactions. In Fig. 1(b), two nanotubes in the unit cell are combined with different rotation angles (0° → 360°) and translation vectors ($0\ b \rightarrow 0.5\ b$). The rotation angle increment is 30° and the translation increment is 0.5 b. This approach is different from methodology employed by Li *et al.* [39], where only the rotated ones of individual nanotubes are considered, thus leading to many feasible combinations being ignored. Upon acquiring all assembly configurations, a set of 50 different structures is planned after careful selection to adhere to crystal symmetry considerations. Subsequently, geometric optimizations of these 50 selected configurations are carried out to obtain the energetically optimal 2D NTs. Figure 1(c) shows the optimized geometric configurations of the P, As, Sb, and Bi 2D NTs with the lowest energy. After optimization, the center of mass of the two nanotubes has a slight difference along the z direction and the rotation angles θ_1 and θ_2 differ by approximately 30°, as indicated by the blue arrows in the nanotube orientations. The second nanotube is translated 0.5 b

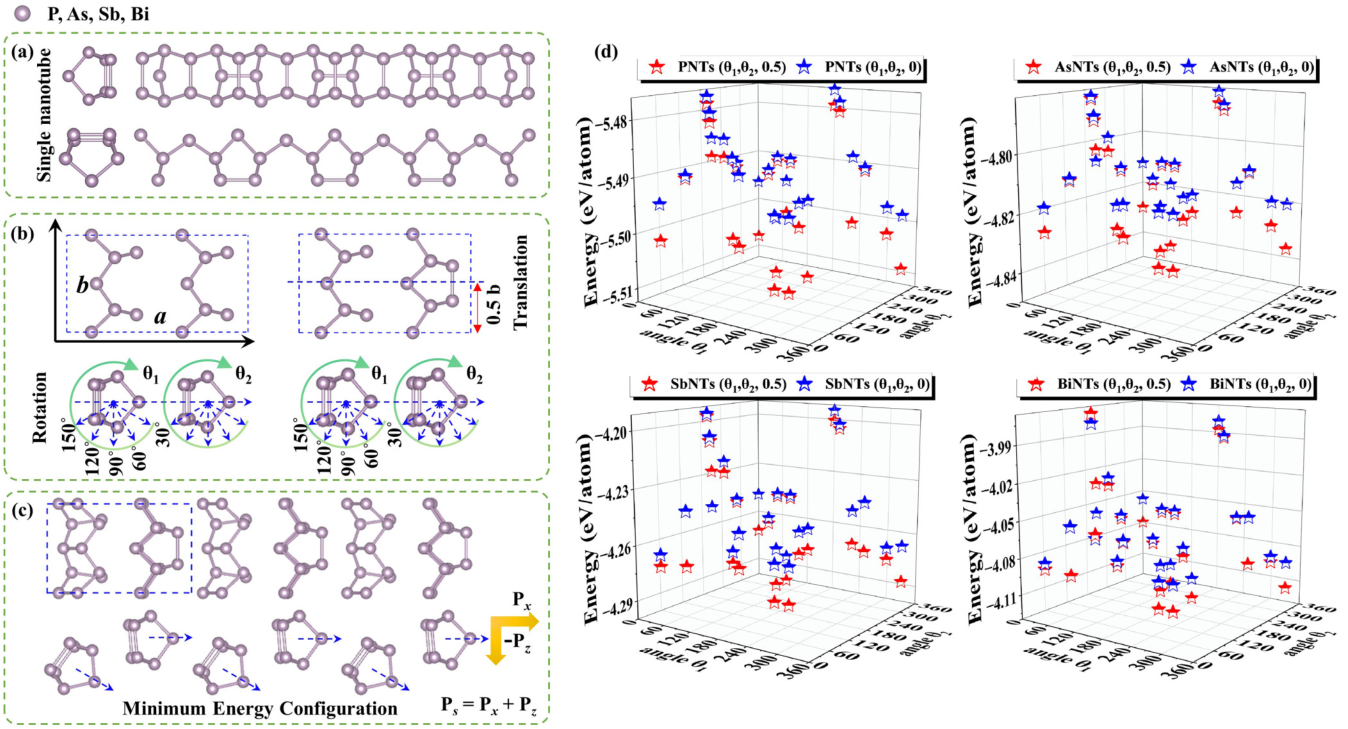

FIG. 1. (a) Schematic diagrams of pentagonal P, As, Sb, and Bi single nanotubes. (b) 2D periodic NTs are assembled from one-dimensional nanotubes at different rotation angles (0° to 360°) and translation vectors (0 *b* to 0.5 *b*). The rotation angle is incremented by 30° and the translation increment is 0.5 *b*. (c) Structure view of the most stable 2D NTs after optimizing all rotational and translational states. (d) Atomic energies of 25 nonequivalent 2D NTs composed of P, As, Sb, and Bi, where red and blue represent the second nanotube in the unit cell of the NTs translated along the lattice vector *b* by 0.5 *b* and 0 *b*, respectively.

along the *b* direction relative to the first nanotube in the lowest energy configuration.

The total energy calculation is shown in Fig. 1(d). It can be observed that, under the same rotation angle, the energy of the configuration with a translation of 0.5 *b* is significantly lower than that without translation. In addition, by performing geometric optimization on configurations with different rotation angles, it is found that several initial structures exhibit energy degeneracy after geometric optimization. A detailed examination of these identical energy structures reveals that they are the identical structures. The per atom energy of the P, As, Sb, and Bi 2D NTs, as shown in Table I. The energy of the P NTs obtained in our study is lower than that of the array proposed by Li *et al.* [39] and the As, Sb, and Bi NTs also share the same configuration as ground state arrangement. Interestingly, the As and P NTs exhibit higher energy stability in comparison to the black phosphorene phase. To ensure reliability in practical applications, the phonon dispersion of individual NTs and 2D NTs lattice dynamical and thermal stability are investigated as shown in Supplemental Material Figs. S1–S3 [53]. There are no imaginary phonon frequencies along the entire highly symmetric Brillouin band path. At 300 K, the system's temperature remains steady, with no significant changes in free energy. Snapshots of the initial and final states show that the NTs remains stable after 10 ps of dynamic evolution. In addition, these NTs also meet the Born-Huang criteria [45,54] (i.e., $C_{11} > 0$, $C_{66} > 0$, and $C_{11} * C_{22} > C_{12}^2$), demonstrating their ability to resist small mechanical deformation, as shown in Table II.

TABLE I. Free energy E_f (eV/atom) of the P, As, Sb, and Bi 2D NTs and black phosphorene phase (BP).

	E_f		
Elements	NTs (in this work)	NTs (Li *et al.* [39])	BP
P	−5.512	−5.509	−5.492
As	−4.842	−4.837	−4.833
Sb	−4.298	−4.289	−4.312
Bi	−4.128	−4.118	−4.167

Based on the intrinsic symmetry, there exists four equivalent most stable configurations of NTs which are labeled as A, B, A′, and B′ shown in Fig. 2(a). Assuming configuration A as the reference starting point and using the rotation angles θ_1 and θ_2 as the *x* and *y* coordinates, the relative positions of A, B, A′, and B′ are visualized as shown in Fig. 2(b). Figure 2(c) represents a simplified model of their interconversion. Typically, the electronic band structures of ferroelectric materials exhibit semiconductor characteristics and remain insulating during the polarization switching process. Therefore, HSE06 [50] and PBE [42] calculations are used to obtain their band structure information and the results are depicted in Fig. 3. As previous studies have been reported, the PBE results always significantly underestimate the band gap of materials. The research results indicate that the NTs belong to indirect band

TABLE II. Relaxed-ion elastic stiffness coefficients C_{ij} and relaxed-ion piezoelectric coefficients e_{ij} and d_{ij}. The units for C_{ij}, e_{ij}, and d_{ij} are N/m, pC/m, and pm/V, respectively.

Elements	C_{11}	C_{22}	C_{12}	C_{66}	e_{11}	e_{12}	e_{31}	e_{32}	d_{11}	d_{12}	d_{31}
P	12.60	109.86	5.79	11.90	12.64	19.28	0.58	1.10	0.95	0.13	0.04
As	15.89	78.17	9.34	13.59	18.08	−30.48	1.58	−0.03	1.47	−0.57	0.12
Sb	18.14	51.78	11.67	13.79	31.7	−51.02	1.22	−1.68	2.78	−1.61	0.10
Bi	20.33	40.65	14.13	11.77	85.18	108.24	105.26	−52.18	7.97	−5.43	8.01

gap semiconductors, with a band gap ranging from 0.89 to 2.58 eV. Furthermore, the band gap decreases gradually with the increase in atomic number of the constituent elements.

Ferroelectric materials play a crucial role in various applications, including nonvolatile memory and logic devices, due to their inherent capability for spontaneous polarization switching [1–3]. Among them, the ferroelectric switch barrier is the polarization switch of ferroelectric materials must overcome. In Fig. 2(a), the direction of each nanotube is marked with a blue arrow. The A and B NTs have an upward OOP orientation, while the A′ and B′ NTs have a downward OOP orientation. According to their symmetry, there are two nonequivalent polarization switching modes, A′ → A and A′ → B (or B′ → A and B′ → B), in the OOP polarized switching process. However, it can be seen from Fig. 2(b) that the displacement transformation from A′ → A is significantly smaller than that from A′ → B during the OOP polarization switching process. Therefore, the OOP polarization flipping path is more likely to be along A′ → A and the two nanotubes within the unit cell rotate in a clockwise direction simultaneously, as shown in Fig. 4(a). The contour image of the free energy during the OOP polarization switching process from A′ to A for P, As, Sb, and Bi NTs is depicted in Fig. 5. Obviously, the two equivalent states, A′ and A, exhibit minimum values and are connected by a saddle point O, which strongly suggests the existence of OOP ferroelectricity. Besides the different OOP orientations, there also exists different IP orientations for A, A′, B, and B′. Similarly, according to the symmetry, two nonequivalent IP polarization switching modes are revealed in NTs as well: A → B and A → B′ (or A′ → B′ and A → B). However, compared with the OOP polarization, IP polarization switching is much more complex. In Fig. 2(b), A → B and A → B′ are almost equidistant; thus it is difficult for us to directly determine the IP polarization switching mode. To simplify the matters, the relative energy barriers on each switch path are preliminarily determined by calculating the free energy of the eight conversion paths, including considering the rotation direction of each nanotube. It can be seen from Fig. S4 in the Supplemental Material [53], for all P, As, Sb, and Bi NTs, the switching energy barrier from A → B (ACW-CW) path is much lower than the other seven paths. The first nanotube rotates counterclockwise and the second nanotube rotates clockwise, as shown in Fig. 4(b).

After identifying the pathways for the OOP and IP polarization switching, the CINEB [51] method is employed to evaluate the energy barrier size for polarization switching. The van der Waals interaction between nanotubes leads to minimal switching energy barriers in the range of tens of meV/atom for 2D NTs composed of P, As, Sb, and Bi. Such behavior places these materials in a category typically associated with low ferroelectric polarization switching energy barriers, a group that encompasses hybrid nonintrinsic ferroelectric materials, ferroelectric 2D materials, and van der Waals materials. The low energy barrier signifies diminished energy demands for polarization switching, ultimately

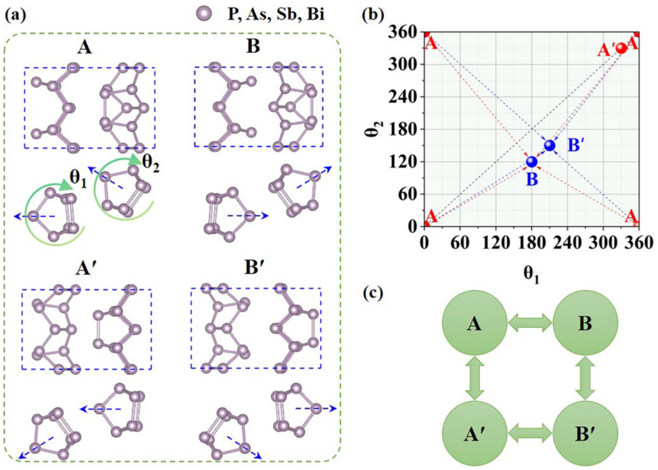

FIG. 2. (a) Four equivalent configurations (A, B, A′, and B′) of the most stable 2D NTs. Panels (b) and (c) depict transitions between these configurations, where configuration A is taken as the reference starting point.

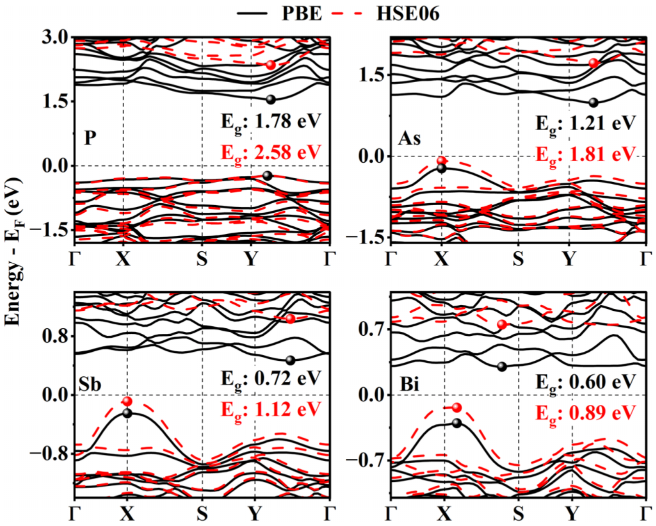

FIG. 3. Electronic band structure of the most stable 2D NTs of P, As, Sb, and Bi is studied, where the positions of the valence band maximum (VBM) and conduction band minimum (CBM) are highlighted with small spheres.

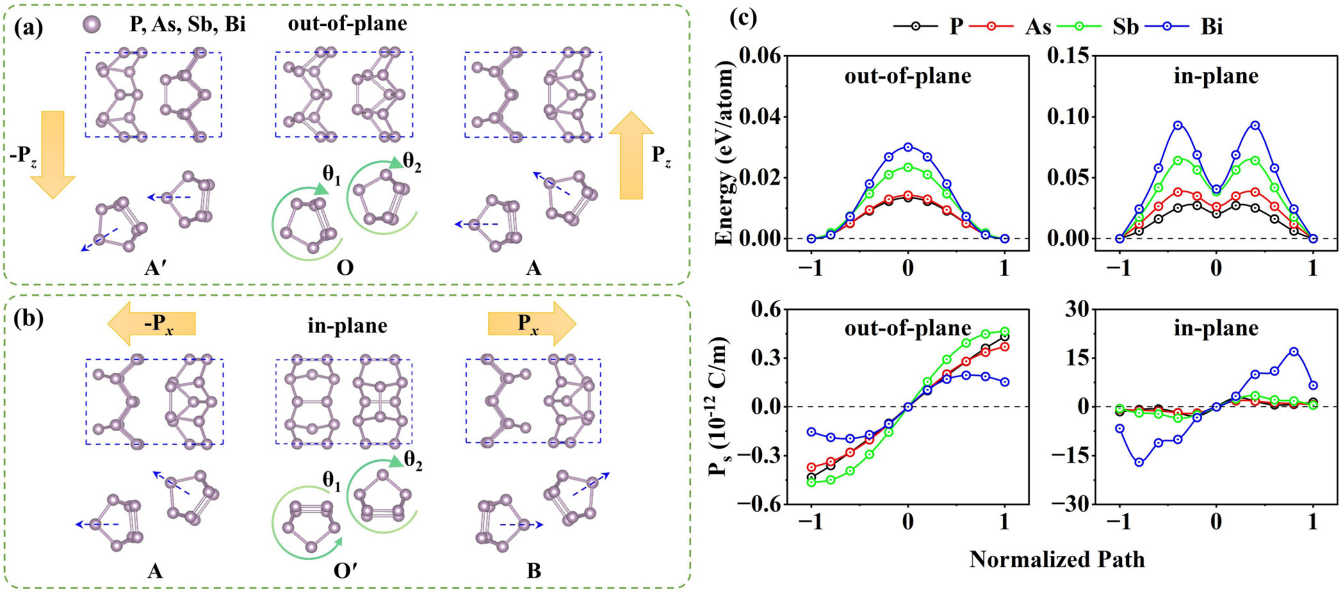

FIG. 4. Schematic diagrams of the (a) OOP and (b) IP polarization switching paths of P, As, Sb, and Bi 2D NTs. (c) The polarization switching barrier and variation of polarization P_s along the path for P, As, Sb, and Bi 2D NTs. The −1 and 1 on the abscissa denote the initial and final states, respectively.

facilitating smoother and more energy-efficient polarization switching processes, leading to faster device response [55]. Consequently, materials with low ferroelectric energy barriers can achieve polarization inversion under lower electric fields, rendering them highly applicable in practical scenarios. For instance, achieving a reduction in the switching energy of ferroelectric thin films has long been a significant objective in the development of ultralow power ferroelectric memories and logic devices. In addition, as shown in Fig. 4(c), the energy barrier for IP polarization switching is considerably higher compared to that of OOP polarization switching.

The most crucial intrinsic property of ferroelectric materials lies in their inherent spontaneous polarization. According to modern polarization theory, the standard Berry's phase [47,48] method can be utilized to calculate the magnitude of spontaneous polarization, P_s, in 2D NTs of P, As, Sb, and Bi. Figure 4(c) depicts the variation of OOP and IP polarization P_s of P, As, Sb, and Bi 2D NTs along the path. During OOP polarization switching, the OOP ferroelectricity gradually diminishes as a result of the mutual rotation of nanotubes. This process undergoes an intermediate phase (designated as O) with a point group of *mm*2, in which the OOP polarization is suppressed while the IP polarization continues to exist. In contrast, during the IP polarization switching, the intermediate phase is O′ with a point group of *mmm*. Both IP and OOP polarizations are simultaneously suppressed at this phase. The magnitudes of OOP polarization for P, As, Sb, and Bi 2D NTs are 0.43, 0.37, 0.47, and 0.15 pC/m, as shown in Table III. Their magnitudes of IP polarization are 1.45, 0.71, 0.51, and 6.63 pC/m, respectively, if the polarization unit is converted to $\mu C/cm^2$. The OOP polarization magnitudes of P, As, Sb, and Bi 2D NTs are 0.048, 0.040, 0.043, and 0.013 $\mu C/cm^2$, respectively, while the IP polarization magnitudes are 0.162, 0.077, 0.048, and 0.571 $\mu C/cm^2$, respectively. Among them, the effective thicknesses of P, As, Sb, and Bi 2D NTs are 8.96, 9.24, 10.87, and 11.61 Å, respectively. These polarization magnitudes are in line with the sizes of some theoretically predicted or experimentally

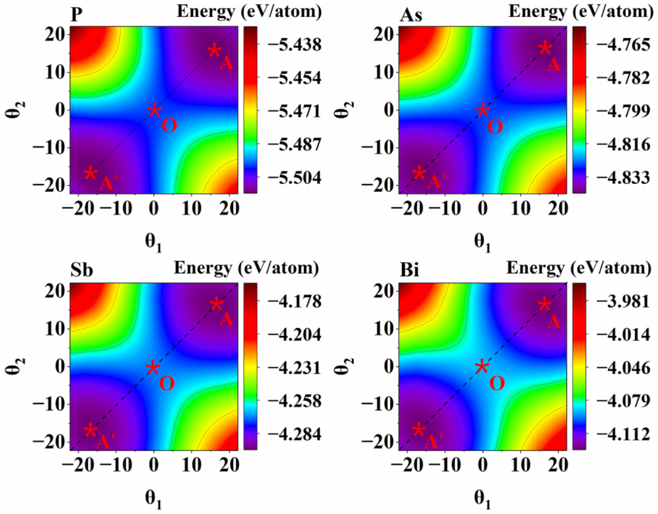

FIG. 5. Contour map of free energy as a function of rotation angles θ_1 and θ_2 during the OOP polarization switching process of P, As, Sb, and Bi 2D NTs, with three phases A′, O, and A marked.

TABLE III. Lattice constant *a* and *b* (Å), OOP and IP spontaneous polarization P_s (pC/m), and OOP and IP polarization switching energy barrier E_b (eV/atom) of the P, As, Sb, and Bi 2D NTs.

Elements	*a*	*b*	P_s (OOP)	P_s (IP)	E_b (OOP)	E_b (IP)
P	10.46	6.48	0.43	1.45	0.013	0.025
As	10.81	7.14	0.37	0.71	0.014	0.038
Sb	11.59	8.15	0.47	0.52	0.023	0.064
Bi	11.71	8.51	0.15	6.63	0.030	0.093

verified sliding ferroelectrics, such as InSe [29] (0.24 pC/m), GaSe [29] (0.46 pC/m), $\mathrm{MoS_2}$ [29] (0.97 pC/m), *h*-BN [29] (2.08 pC/m), $\mathrm{WTe_2}$ [56–59] (0.051 $\mu\mathrm{C/cm^2}$), and graphene-based Moiré heterostructures [60] (0.05 $\mu\mathrm{C/cm^2}$). It is crucial to note that P, As, Sb, and Bi 2D NTs exhibit both IP and OOP polarizations, unlike most 2D ferroelectric materials that possess only one polarization direction [14,18,20,32,61,62] (usually with IP polarization). In fact, the depolarization field is generated due to the presence of uncompensated surface charges, which is energetically unfavorable for the ferroelectricity of nanostructures [63–65]. However, compared with the NTs without OOP polarization proposed by Li *et al.* [39], our proposed NTs with coexisting OOP and IP have a lower energy advantage, as shown in Table I. In addition, these 2D van der Waals NTs have clean surfaces, no dangling bonds, and a saturated interface chemical environment. These characteristics make their OOP polarization less susceptible to destruction by the depolarization field. As a result, these 2D NTs possess four logical states, which can be described as 0, 1, 2, and 3, thereby allowing for the storage of more information when integrated into micro/nanodevice systems. For example, a memory device integrated with n transistors can store information of 2^n based on logical states of 0 and 1, whereas the device utilizing 0, 1, 2, and 3 logical states can store information of 4^n. In addition, the ability of ferroelectric materials to maintain their ferroelectric properties above room temperature is crucial. At room temperature, the OOP polarization magnitudes of thermal average structure (see Fig. S5 of the Supplemental Material [53]) of P, As, Sb, and Bi 2D NTs are 0.60, 0.43, 0.62, and 0.25 pC/m, respectively, and the IP polarization magnitudes are 1.50, 0.72, 0.39, and 5.28 pC/m, respectively.

Obviously, unlike traditional displacive ferroelectrics where the polarization arises from the asymmetric placement of cations and anions, there is no electronegativity difference between the elements of the 2D NTs composed of P, As, Sb, and Bi, as shown in Fig. 1. However, the polarization phenomenon in these single-element 2D NTs is of particular interest. From the perspective of crystal point group symmetry, they all belong to the m point group, satisfying the necessary condition of point group for ferroelectricity, i.e., breaking of centrosymmetry. The electron localization function, average charge density distribution, and average electrostatic potential distribution are plotted in Fig. 6(a); it can be observed that the electron localization function exhibits obvious localized lone pair on the P, As, Sb, and Bi 2D NTs, clearly showing the accumulation and depletion of charge around each atom. This disruption of electron distribution symmetry leads to the formation of positive and negative charge centers, inducing the spontaneous generation of an electric dipole moment within the crystal material. The polarization direction is dependent on the orientation arrangement of the nanotubes. Moreover, a clearer understanding of the inhomogeneity in charge distribution and the displayed polarization field within these NTs is possible by referring to Figs. 6(b) and 6(c). These results enhance our comprehension of the factors underlying polarization in the single-element P, As, Sb, and Bi 2D NTs.

It is well known that ferroelectric materials always possess piezoelectricity. For the 2D materials, the dimensions of the piezoelectric coefficient matrix, the e_{ij} and d_{ij} tensors, transform from a 3×6 matrix in a three-dimensional state to a 3×3 matrix. According to the definition, the d_{ij} tensor represents the strain generated by applied electric field, while the e_{ij} tensor represents the polarization change caused by strain [66]. In Voigt notation, the subscripts $i = 1$, 2, and 3 in e_{ij} and d_{ij} tensors denote the x, y, and z directions and $j = 1$, 2, and 6 denote the xx, yy, and xy directions, respectively. For example, e_{31} represents the response strength of polarization change in the z direction induced by strain applied in the xx direction. For the m point group, the independent nonzero matrix elements in its e_{ij} and d_{ij} matrices are e_{11}, e_{12}, e_{26}, e_{31}, e_{32} and d_{11}, d_{12}, d_{26}, d_{31}, d_{32}. Therefore, the piezoelectric coefficient matrix is represented as

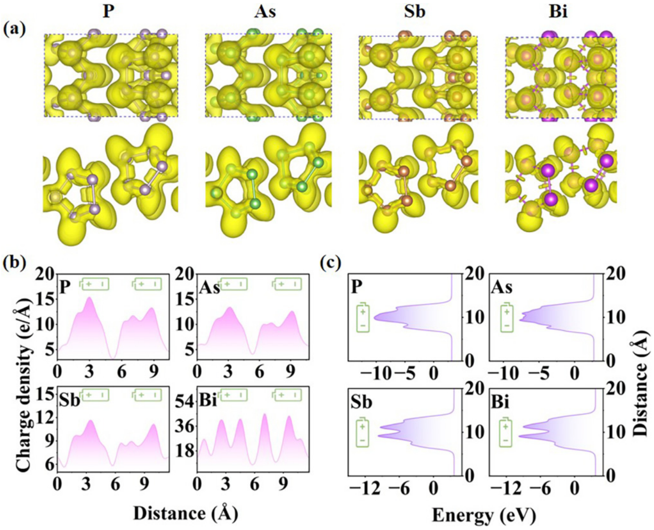

FIG. 6. (a) Three-dimensional electron localization function, (b) average charge density distribution along lattice a direction, and (c) average electrostatic potential distribution along lattice z direction of 2D NTs of P, As, Sb, and Bi.

$$e_{ij} = \begin{pmatrix} e_{11} & e_{12} & 0 \\ 0 & 0 & e_{26} \\ e_{31} & e_{32} & 0 \end{pmatrix}, \tag{1}$$

$$d_{ij} = \begin{pmatrix} d_{11} & d_{12} & 0 \\ 0 & 0 & d_{26} \\ d_{31} & d_{32} & 0 \end{pmatrix}. \tag{2}$$

Furthermore, for 2D materials in the orthogonal crystal system, the four independent elastic stiffness coefficients are denoted as C_{11}, C_{12}, C_{22}, and C_{66}, respectively [45]:

$$C_{ij} = \begin{pmatrix} C_{11} & C_{12} & 0 \\ C_{12} & C_{22} & 0 \\ 0 & 0 & C_{66} \end{pmatrix}. \tag{3}$$

Here, we mainly focus on d_{11}, d_{12}, and d_{31} and, according to $d_{ij} = e_{ij}C_{ij}^{-1}$,

$$d_{11} = \frac{e_{11}C_{22} - e_{12}C_{12}}{C_{11}C_{22} - C_{12}^2}, \quad d_{12} = \frac{e_{12}C_{11} - e_{11}C_{12}}{C_{11}C_{22} - C_{12}^2},$$

$$d_{31} = \frac{e_{31}C_{22} - e_{32}C_{12}}{C_{11}C_{22} - C_{12}^2}. \tag{4}$$

The relaxed-ion piezoelectric coefficients e_{ij} and d_{ij} are calculated using the DFPT method as illustrated in Table II. The d_{ij} coefficients displayed a periodic trend, consistent with the periodicity observed in the piezoelectric coefficients of some binary compounds, where the piezoelectric coefficients increase with the atomic number of the elements [67,68]. Interestingly, single-element P, As, Sb, and Bi NTs exhibit outstanding piezoelectric performance, with d_{11} ranging from 0.95 to 7.97 pm/V. The reason behind this phenomenon can be understood from the algebraic expression of the piezoelectric coefficients d_{ij}. The electron localizations depicted in Fig. 6(a) show that, in the lattice direction a, the nanotubes are primarily stabilized by van der Waals forces, while in the lattice direction b, the elements are interconnected by strong covalent bonds. This leads to smaller C_{11} and larger C_{22} values. Therefore, due to the combined effect of significant e_{11} resulting from the asymmetric electron distribution and the significant difference between C_{11} and C_{22}, elemental P, As, Sb, and Bi 2D NTs exhibit excellent piezoelectric coefficients, even surpassing those of some common 2D piezoelectric materials like MoS_2 (3.65 pm/V), WS_2 (2.12 pm/V), InSe (1.98 pm/V), and h-BN (0.61 pm/V) [69]. Moreover, they also possess nonzero OOP piezoelectric coefficients d_{31}, ranging from 0.04 to 8.01 pm/V. These coefficients describe the piezoelectric effect of polarization changes perpendicular to the atomic plane induced by stress or strain in the 2D material. The existence of perpendicular polarization enables the use of these materials in a wider array of 2D piezoelectric applications [70]. For example, 2D piezoelectric materials exhibiting OOP piezoelectric response are particularly suitable for applications involving ultrathin piezoelectric devices [71]. Additionally, these nonzero d_{11} and d_{31} coefficients reflect the tunability of both IP and OOP polarization under the influence of stress or strain.

IV. CONCLUSION

In this study, we design a unique nanotube featuring pentagonal units that are meticulously composed of individual group-V elements (P, As, Sb, and Bi). These configurations exhibit fundamental structural units strikingly akin to violet phosphorus and fibrous red phosphorus. After assembling these nanotubes into a 2D array, each nanotube is systematically rotated to attain its optimal energetic configuration. The obtained NTs exhibit exceptional mechanical, lattice dynamical, and thermal stability. Our investigation unveils that these NTs exhibit semiconductor attributes, characterized by an indirect band gap spanning 0.89 to 2.58 eV. Most importantly, these NTs manifest simultaneous IP and OOP spontaneous polarizations, a rarity among elemental ferroelectric materials. It is crucial to note that this ferroelectricity remains intact even at room temperature. The OOP spontaneous polarizations for P, As, Sb, and Bi are evaluated at 0.43, 0.37, 0.47, and 0.15 pC/m, respectively, while the IP spontaneous polarizations stand at 1.45, 0.71, 0.51, and 6.63 pC/m. The coexistence of IP and OOP polarizations yields four equivalent polarization configurations, denoted as 0, 1, 2, and 3 in logical gates. Such multipolarization state could significantly augment the data storage density in ferroelectric memory devices. Moreover, we demonstrate that transitioning between these multipolarization states is feasible with minimal switching barriers, typically within the range of a few tens of meV/atom. The low ferroelectric polarization switching barrier implies susceptibility to external electric fields, enabling faster data read-write operations and reduced energy consumption. Moreover, the presence of a nonzero OOP piezoelectric coefficient (d_{31}) alongside IP piezoelectric properties surpassing those of h-BN and rivaling MoS_2 also enhances the potential of these 2D NTs in piezoelectric applications. These significant findings pave avenues to realize ferroelectricity in single-element materials and furnish valuable theoretical insights for devising high-capacity ferroelectric storage devices.

ACKNOWLEDGMENTS

This work is supported by the National Natural Science Foundation of China (Grants No. 52372260, No. 11974299, No. 12204397, and No. 11974300), the Youth Science and Technology Talent Project of Hunan Province (Grant No. 2022RC1197), the Science Fund for Distinguished Young Scholars of Hunan Province of China (Grant No. 2021JJ10036), and the Hunan Provincial Innovation Foundation for Postgraduate (Grant No. CX20220544).

---

[1] D. Zhang, D. Sando, P. Sharma, X. Cheng, F. Ji, V. Govinden, M. Weyland, V. Nagarajan, and J. Seidel, Superior polarization retention through engineered domain wall pinning, Nat. Commun. **11**, 349 (2020).

[2] L. W. Martin and A. M. Rappe, Thin-film ferroelectric materials and their applications, Nat. Rev. Mater. **2**, 16087 (2016).

[3] Z. Guan, H. Hu, X. W. Shen, P. H. Xiang, N. Zhong, J. H. Chu, and C. G. Duan, Recent progress in two-dimensional ferroelectric materials, Adv. Electron. Mater. **6**, 1900818 (2020).

[4] J. Valasek, Piezo-electric and allied phenomena in rochelle salt, Phys. Rev. **17**, 475 (1921).

[5] M. Wu, 100 years of ferroelectricity, Nat. Rev. Phys. **3**, 726 (2021).

[6] N. Setter, D. Damjanovic, L. Eng, G. Fox, S. Gevorgian, S. Hong, A. Kingon, H. Kohlstedt, N. Y. Park, G. B. Stephenson, I. Stolitchnov, A. K. Taganstev, D. V. Taylor, T. Yamada, and S. Streiffer, Ferroelectric thin films: Review of materials, properties, and applications, J. Appl. Phys. **100**, 051606 (2006).

[7] C. H. Ahn, K. M. Rabe, and J. M. Triscone, Ferroelectricity at the nanoscale: Local polarization in oxide thin films and heterostructures, Science **303**, 488 (2004).

[8] M. Dawber, K. M. Rabe, and J. F. Scott, Physics of thin-film ferroelectric oxides, Rev. Mod. Phys. **77**, 1083 (2005).

[9] H. Wang, Z. R. Liu, H. Y. Yoong, T. R. Paudel, J. X. Xiao, R. Guo, W. N. Lin, P. Yang, J. Wang, G. M. Chow, T. Venkatesan, E. Y. Tsymbal, H. Tian, and J. S. Chen, Direct observation of room-temperature out-of-plane ferroelectricity and tunneling electroresistance at the two-dimensional limit, Nat. Commun. **9**, 3319 (2018).

[10] D. D. Fong, G. B. Stephenson, S. K. Streiffer, J. A. Eastman, O. Auciello, P. H. Fuoss, and C. Thompson, Ferroelectricity in ultrathin perovskite films, Science **304**, 1650 (2004).

[11] J. Junquera and P. Ghosez, Critical thickness for ferroelectricity in perovskite ultrathin films, Nature (London) **422**, 506 (2003).

[12] T. Jin, J. Mao, J. Gao, C. Han, K. P. Loh, A. T. S. Wee, and W. Chen, Ferroelectrics-integrated two-dimensional devices toward next-generation electronics, ACS Nano **16**, 13595 (2022).

[13] C. Yang, M. Chen, S. Li, X. Zhang, C. Hua, H. Bai, C. Xiao, S. A. Yang, P. He, Z.-A. Xu, and Y. Lu, Coexistence of ferroelectricity and ferromagnetism in one-dimensional SbN and BiN nanowires, ACS Appl. Mater. Interfaces **13**, 13517 (2021).

[14] K. Chang, J. Liu, H. Lin, N. Wang, K. Zhao, A. Zhang, F. Jin, Y. Zhong, X. Hu, W. Duan, Q. Zhang, L. Fu, Q. K. Xue, X. Chen, and S. H. Ji, Discovery of robust in-plane ferroelectricity in atomic-thick SnTe, Science **353**, 274 (2016).

[15] W. Ding, J. Zhu, Z. Wang, Y. Gao, D. Xiao, Y. Gu, Z. Zhang, and W. Zhu, Prediction of intrinsic two-dimensional ferroelectrics in In_2Se_3 and other III_2-VI_3 van der Waals materials, Nat. Commun. **8**, 14956 (2017).

[16] Y. Zhou, D. Wu, Y. Zhu, Y. Cho, Q. He, X. Yang, K. Herrera, Z. Chu, Y. Han, M. C. Downer, H. Peng, and K. Lai, Out-of-plane piezoelectricity and ferroelectricity in layered alpha-In2Se3 nanoflakes, Nano Lett. **17**, 5508 (2017).

[17] A. Belianinov, Q. He, A. Dziaugys, P. Maksymovych, E. Eliseev, A. Borisevich, A. Morozovska, J. Banys, Y. Vysochanskii, and S. V. Kalinin, $CuInP_2S_6$ room temperature layered ferroelectric, Nano Lett. **15**, 3808 (2015).

[18] F. Liu, L. You, K. L. Seyler, X. Li, P. Yu, J. Lin, X. Wang, J. Zhou, H. Wang, H. He, S. T. Pantelides, W. Zhou, P. Sharma, X. Xu, P. M. Ajayan, J. Wang, and Z. Liu, Room-temperature ferroelectricity in CuInP2S6 ultrathin flakes, Nat. Commun. **7**, 12357 (2016).

[19] S. N. Shirodkar and U. V. Waghmare, Emergence of ferroelectricity at a metal-semiconductor transition in a 1t monolayer of MoS_2, Phys. Rev. Lett. **112**, 157601 (2014).

[20] R. Fei, W. Kang, and L. Yang, Ferroelectricity and phase transitions in monolayer group-iv monochalcogenides, Phys. Rev. Lett. **117**, 097601 (2016).

[21] Z. Li, Y. Gu, C. He, and X. Zou, Fully auxetic and multifunctional of two-dimensional δ-GeS and δ-GeSe, Phys. Rev. B **106**, 035426 (2022).

[22] S. Song, Y. Zhang, J. Guan, and S. Dong, Noncollinear ferrielectricity and morphotropic phase boundary in monolayer GeS, Phys. Rev. B **103**, L140104 (2021).

[23] N. Higashitarumizu, H. Kawamoto, C. J. Lee, B. H. Lin, F. H. Chu, I. Yonemori, T. Nishimura, K. Wakabayashi, W. H. Chang, and K. Nagashio, Purely in-plane ferroelectricity in monolayer SnS at room temperature, Nat. Commun. **11**, 2428 (2020).

[24] X. Tang and L. Kou, Two-Dimensional ferroics and multiferroics: Platforms for new physics and applications, J. Phys. Chem. Lett. **10**, 6634 (2019).

[25] B. Behera, B. C. Sutar, and N. R. Pradhan, Recent progress on 2D ferroelectric and multiferroic materials, challenges, and opportunity, Emergent Mater. **4**, 847 (2021).

[26] F. Sui, M. Jin, Y. Zhang, R. Qi, Y.-N. Wu, R. Huang, F. Yue, and J. Chu, Sliding ferroelectricity in van der Waals layered γ-InSe semiconductor, Nat. Commun. **14**, 36 (2023).

[27] L. Yang and M. Wu, Across-Layer sliding ferroelectricity in 2d heterolayers, Adv. Funct. Mater. **33**, 2301105 (2023).

[28] M. Vizner Stern, Y. Waschitz, W. Cao, I. Nevo, K. Watanabe, T. Taniguchi, E. Sela, M. Urbakh, O. Hod, and M. Ben Shalom, Interfacial ferroelectricity by van der Waals sliding, Science **372**, 1462 (2021).

[29] L. Li and M. Wu, Binary compound bilayer and multilayer with vertical polarizations: Two-dimensional ferroelectrics, multiferroics, and nanogenerators, ACS Nano **11**, 6382 (2017).

[30] T. Zhang, Y. Liang, X. Xu, B. Huang, Y. Dai, and Y. Ma, Ferroelastic-ferroelectric multiferroics in a bilayer lattice, Phys. Rev. B **103**, 165420 (2021).

[31] Y. Zhang, T. Ouyang, C. He, J. Li, and C. Tang, Extremely promising monolayer materials with robust ferroelectricity and extraordinary piezoelectricity: δ-AsN, δ-SbN, and δ-BiN, Nanoscale **15**, 6363 (2023).

[32] C. C. Xiao, F. Wang, S. Y. A. Yang, Y. H. Lu, Y. P. Feng, and S. B. Zhang, Elemental ferroelectricity and antiferroelectricity in group-v monolayer, Adv. Funct. Mater. **28**, 1707383 (2018).

[33] J. Gou, H. Bai, X. Zhang, Y. L. Huang, S. Duan, A. Ariando, S. A. Yang, L. Chen, Y. Lu, and A. T. S. Wee, Two-dimensional ferroelectricity in a single-element bismuth monolayer, Nature (London) **617**, 67 (2023).

[34] D. Liu, J. Guan, J. Jiang, and D. Tománek, Unusually stable helical coil allotrope of phosphorus, Nano Lett. **16**, 7865 (2016).

[35] G. Schusteritsch, M. Uhrin, and C. J. Pickard, Single-layered hittorf's phosphorus: A wide-bandgap high mobility 2d material, Nano Lett. **16**, 2975 (2016).

[36] L. Zhang, H. Huang, B. Zhang, M. Gu, D. Zhao, X. Zhao, L. Li, J. Zhou, K. Wu, Y. Cheng, and J. Zhang, Structure and properties of violet phosphorus and its phosphorene exfoliation, Angew. Chem. Int. Ed. **59**, 1074 (2020).

[37] M. Ruck, D. Hoppe, B. Wahl, P. Simon, Y. Wang, and G. Seifert, Fibrous red phosphorus, Angew. Chem., Int. Ed. **44**, 7616 (2005).

[38] J. Zhang, D. Zhao, D. Xiao, C. Ma, H. Du, X. Li, L. Zhang, J. Huang, H. Huang, C. L. Jia, D. Tomanek, and C. Niu, Assembly of ring-shaped phosphorus within carbon nanotube nanoreactors, Angew. Chem. Int. Ed. **56**, 1850 (2017).

[39] Z. Li, C. He, T. Ouyang, C. Zhang, C. Tang, R. A. Römer, and J. Zhong, Allotropes of phosphorus with remarkable stability and intrinsic piezoelectricity, Phys. Rev. Appl. **9**, 044032 (2018).

[40] G. Kresse and J. Furthmüller, Efficient iterative schemes for *ab initio* total-energy calculations using a plane-wave basis set, Phys. Rev. B **54**, 11169 (1996).

[41] P. E. Blöchl, Projector augmented-wave method, Phys. Rev. B **50**, 17953 (1994).

[42] G. Kresse and D. Joubert, From ultrasoft pseudopotentials to the projector augmented-wave method, Phys. Rev. B **59**, 1758 (1999).

[43] J. P. Perdew, K. Burke, and M. Ernzerhof, Generalized gradient approximation made simple, Phys. Rev. Lett. **77**, 3865 (1996).

[44] H. J. Monkhorst and J. D. Pack, Special points for Brillouin-zone integrations, Phys. Rev. B **13**, 5188 (1976).

[45] V. Wang, N. Xu, J.-C. Liu, G. Tang, and W.-T. Geng, VASPKIT: A user-friendly interface facilitating high-throughput computing and analysis using VASP code, Comput. Phys. Commun. **267**, 108033 (2021).

[46] S. Grimme, Semiempirical GGA-type density functional constructed with a long-range dispersion correction, J. Comput. Chem. **27**, 1787 (2006).

[47] D. Vanderbilt, Berry-phase theory of proper piezoelectric response, J. Phys. Chem. Solids **61**, 147 (2000).

[48] R. D. King-Smith and D. Vanderbilt, Theory of polarization of crystalline solids, Phys. Rev. B **47**, 1651 (1993).

[49] X. Wu, D. Vanderbilt, and D. R. Hamann, Systematic treatment of displacements, strains, and electric fields in density-functional perturbation theory, Phys. Rev. B **72**, 035105 (2005).

[50] J. Heyd, G. E. Scuseria, and M. Ernzerhof, Hybrid functionals based on a screened coulomb potential, J. Chem. Phys. **118**, 8207 (2003).

[51] G. Henkelman, B. P. Uberuaga, and H. Jónsson, A climbing image nudged elastic band method for finding saddle points and minimum energy paths, J. Chem. Phys. **113**, 9901 (2000).

[52] A. Togo and I. Tanaka, First principles phonon calculations in materials science, Scr. Mater. **108**, 1 (2015).

[53] See Supplemental Material at http://link.aps.org/supplemental/10.1103/PhysRevB.108.245416 for the phonon dispersion, *ab initio* molecular dynamics simulations, preliminary evaluation of the in-plane polarization switching paths, and thermal average structure of 2D NTs.

[54] M. Born and K. Huang, Dynamical theory of crystal lattices, Am. J. Phys. **23**, 474 (1955).

[55] S. Li and T. Birol, Suppressing the ferroelectric switching barrier in hybrid improper ferroelectrics, npj Comput. Mater. **6**, 168 (2020).

[56] Q. Yang, M. Wu, and J. Li, Origin of two-dimensional vertical ferroelectricity in $\mathrm{WTe_2}$ bilayer and multilayer, J. Phys. Chem. Lett. **9**, 7160 (2018).

[57] Z. Fei, W. Zhao, T. A. Palomaki, B. Sun, M. K. Miller, Z. Zhao, J. Yan, X. Xu, and D. H. Cobden, Ferroelectric switching of a two-dimensional metal, Nature (London) **560**, 336 (2018).

[58] P. Sharma, F. X. Xiang, D. F. Shao, D. Zhang, E. Y. Tsymbal, A. R. Hamilton, and J. Seidel, A room-temperature ferroelectric semimetal, Sci. Adv. **5**, eaax5080 (2019).

[59] J. Xiao, Y. Wang, H. Wang, C. D. Pemmaraju, S. Wang, P. Muscher, E. J. Sie, C. M. Nyby, T. P. Devereaux, X. Qian, X. Zhang, and A. M. Lindenberg, Berry curvature memory through electrically driven stacking transitions, Nat. Phys. **16**, 1028 (2020).

[60] Z. Zheng, Q. Ma, Z. Bi, S. de la Barrera, M. H. Liu, N. Mao, Y. Zhang, N. Kiper, K. Watanabe, T. Taniguchi, J. Kong, W. A. Tisdale, R. Ashoori, N. Gedik, L. Fu, S. Y. Xu, and P. Jarillo-Herrero, Unconventional ferroelectricity in moire heterostructures, Nature (London) **588**, 71 (2020).

[61] W. Wan, C. Liu, W. Xiao, and Y. Yao, Promising ferroelectricity in 2D group IV tellurides: A first-principles study, Appl. Phys. Lett. **111**, 132904 (2017).

[62] C. Liu, W. Wan, J. Ma, W. Guo, and Y. Yao, Robust ferroelectricity in two-dimensional SbN and BiP, Nanoscale **10**, 7984 (2018).

[63] K. F. Garrity, K. M. Rabe, and D. Vanderbilt, Hyperferroelectrics: Proper ferroelectrics with persistent polarization, Phys. Rev. Lett. **112**, 127601 (2014).

[64] P. S. Ghosh, D. DeTellem, J. Ren, S. Witanachchi, S. Ma, S. Lisenkov, and I. Ponomareva, Unusual properties of hydrogen-bonded ferroelectrics: The case of cobalt formate, Phys. Rev. Lett. **128**, 077601 (2022).

[65] S. Zhou, J. Zhang, and A. M. Rappe, Strain-induced antipolar phase in hafnia stabilizes robust thin-film ferroelectricity, Sci. Adv. **8**, eadd5953 (2022).

[66] Y. Zhang, T. Ouyang, C. He, J. Li, and C. Tang, Monolayer group-V binary compounds ψ-BiP and ψ-SbP with ultrahigh piezoelectricity and stability, Phys. Rev. Mater. **7**, 016001 (2023).

[67] H. Yin, J. Gao, G.-P. Zheng, Y. Wang, and Y. Ma, Giant piezoelectric effects in monolayer group-v binary compounds with honeycomb phases: A first-principles prediction, J. Phys. Chem. C **121**, 25576 (2017).

[68] R. Fei, W. Li, J. Li, and L. Yang, Giant piezoelectricity of monolayer group IV monochalcogenides: SnSe, SnS, GeSe, and GeS, Appl. Phys. Lett. **107**, 173104 (2015).

[69] Q. Zhang, S. Zuo, P. Chen, and C. Pan, Piezotronics in two-dimensional materials, InfoMat **3**, 987 (2021).

[70] M. N. Blonsky, H. L. Zhuang, A. K. Singh, and R. G. Hennig, Ab initio prediction of piezoelectricity in two-dimensional materials, ACS Nano **9**, 9885 (2015).

[71] S.-D. Guo, X.-S. Guo, Y.-T. Zhu, and Y.-S. Ang, Predicted ferromagnetic monolayer CrSCl with large vertical piezoelectric response: A first-principles study, Appl. Phys. Lett. **121**, 062403 (2022).